ORIGINAL ARTICLE

Characterizing extreme drought and wetness in Guangdong, China using global navigation satellite system and precipitation data

Hai Zhu[1], Kejie Chen[1*] , Haishan Chai[1], Yuanbin Ye[2] and Wenjian Liu[2]

Abstract

As global temperature rises, the frequency of extreme climate events, e.g., severe droughts and floods, has increased significantly and caused severe damage over the past years. To this regard, precipitation efficiency, a crucial meteorological parameter, could provide valuable insights for a better understanding of the patterns and characteristics of these extreme events. In this study, taking Guangdong province as an exemplary region, we first obtained long-term and high-resolution historical records of precipitation efficiency by integrating the observations from a dense network of Global Navigation Satellite System (GNSS) stations with precipitation data, and then characterized the extreme drought and wetness through climate indices. We found a distinct seasonal trend in precipitation efficiency in Guangdong, with annual fluctuations ranging from 10 to 25%. Notably, precipitation efficiency is higher in proximity to the Pearl River Delta Plain and gradually decreases towards the east and west. The occurrence of anomalous peaks and valleys in precipitation efficiency generally corresponds to dry and wet conditions, respectively. A total of 9 extreme wet events and 6 dry events occurred from January 2007 to May 2022, with durations from 3 to 6 months. Our results also demonstrated that both wet and dry frequencies exhibit an increasing trend with the expansion of the time scale, and the frequency of extreme events near the Pearl River Delta Plain surpasses that of other regions. Furthermore, the propagation time from meteorological anomalies to agricultural and hydrological anomalies is about 3 months. The periodic characteristics of meteorological anomalies are identified as the primary driver for other anomalous periodic patterns. Our work unveils the long-term dynamic behavior of precipitation efficiency, as well as the characteristics of extreme drought and wetness events in the regions characterized by intricate land–atmosphere interactions.

Keywords GNSS, Precipitation efficiency, Extreme drought and wetness

Introduction

In the context of global change, the frequency of extreme climate events, such as severe drought and excessive precipitation, is on the rise (e.g., Diffenbaugh et al., 2017; Stott, 2016). Water vapor, a critical greenhouse gas and an integral part of the climate system, serves as a key feedback mechanism (e.g., Chung et al., 2014; Ingram, 2010). The transportation of water vapor involves the transfer of energy in the form of latent heat, which is released as sensible heat when

*Correspondence:
Kejie Chen
chenkj@sustech.edu.cn
[1] Department of Earth and Space Sciences, Southern University of Science and Technology, Shenzhen 518055, China
[2] Lands and Resource Department of Guangdong Province, Surveying and Mapping Institute, Guangzhou 510500, China

Zhu *et al. Satellite Navigation*   (2024) 5:1

Page 2 of 17

condensation occurs (e.g., Jacob, 2001; Schneider et al., 2010). As a result, the diverse processes involving water vapor significantly impact the Earth's energy balance and consequently influence climate change dynamics (Rocken et al., 1997). Extensive research indicates that as climate change advances, both the temperature and water holding capacity in the troposphere increase, leading to an elevation in the actual water vapor content (e.g., Pall et al., 2007; O'Gorman & Schneider, 2009; J. Wang et al., 2016a, 2016b, 2016c). Water vapor, serving as the primary contributor to cloud formation and precipitation, exhibits significant temporal and spatial fluctuations, with its concentration commonly believed to correlate positively with extreme events (e.g., O'Gorman, 2015; Trenberth et al., 2003). Therefore, to effectively mitigate the detrimental effects of extreme drought and wetness events, it is of utmost importance to employ precise monitoring techniques to track the changes in water vapor and to conduct a comprehensive investigation on the conversion rate between water vapor and actual precipitation.

While the influential role of elevated water vapor content on precipitation is widely recognized, the complex intrinsic relationship between precipitation and water vapor still remains unclear (e.g., Benevides et al., 2015; Bordi et al., 2015; Zhao et al., 2020a, 2020b). As stated in Tuller (1973), the occurrence of precipitation in a given region is primarily influenced by three factors: atmospheric water vapor content, the degree of saturation, and the presence of a conductive dynamic mechanism that facilitates the necessary cooling to elevate the saturation level, thereby enabling precipitation. Consequently, this fundamental reason accounts for the observed limited correlation between water vapor and precipitation (Jadala et al., 2022). The intensity of precipitation, particularly during extreme events, is contingent upon the availability of moisture (Trenberth et al., 2003). In this context, Precipitation Efficiency (PE) serves as a widely employed metric in appraising the effectiveness of dynamic precipitation mechanisms, underscoring the paramount importance of available moisture and these mechanisms in precipitation generation (e.g., Doswell et al., 1996; Sui et al., 2007). Specifically, PE is quantified as the ratio of the atmospheric water vapor above a specific station that condenses to the precipitates onto the Earth's surface (Tuller, 1971). The utilization of PE as a characterization tool offers valuable insights into the underlying mechanisms driving extreme drought and wetness events (e.g., Ye et al., 2014; R. L. Li et al., 2023). By quantifying the transformation of atmospheric water vapor into precipitation at a given location, PE facilitates a better understanding of the precipitation generation mechanisms (e.g., R. L. Li et al., 2022; Yin et al., 2022). This insight is

particularly crucial in the regions susceptible to frequent or prolonged droughts and heavy wetness events.

High-resolution water vapor information is indispensable for understanding PE's substantial temporal and spatial variability. Currently, various conventional techniques exist for retrieving water vapor, including radiosonde, water vapor radiometers, satellite remote sensing, and global satellite navigation systems (e.g., Jade et al., 2005; Zhao et al., 2022). Radiosonde networks have traditionally served as the primary means of acquiring data for water vapor monitoring. However, despite the high accuracy of water vapor measurements obtained with radiosonde, data scarcity remains a prevalent issue in many regions (e.g., Ohtani & Naito, 2000; Q. Zhang et al., 2018). Although water vapor radiometers can enhance temporal resolution, their widespread utilization is hindered by the associated high costs (B. Zhang & Yao, 2021). While spatial remote sensing excels in spatial resolution for water vapor retrieval, its accuracy is susceptible to weather conditions and ground factors, introducing significant uncertainties (e.g., Gao & Kaufman, 2003; Z. Liu et al., 2013). In comparison, the Global Navigation Satellite System (GNSS) network surpasses other observation methods by providing superior temporal and spatial resolution, longer time series, and precise information on water vapor changes (e.g., Bevis et al., 1992; X. Li et al., 2015; Huang et al., 2021). Drawing upon these inherent advantages, numerous studies have endeavored to integrate GNSS data with precipitation measurements to estimate PE (e.g., Bordi et al., 2014; Zhu, Chen, Hu, Liu, et al., 2023). This integration holds the potential to provide precise and dependable distribution maps of PE, thereby facilitating investigations on extreme events with higher accuracy and reliability.

Given the intricate spatial variability of PE across diverse regions, undertaking specific investigations becomes imperative (Wang et al., 2019). Guangdong, located in the southeastern coastal area of China, emerges as a region distinguished by notable fluctuations in water vapor and frequent interactions between land and air. During the summer and autumn, the monsoon airflow transports abundant quantities of warm and humid water vapor from the tropical Indian Ocean and the South China Sea to the East Asian continent, resulting in substantial precipitation in Guangdong. The province is susceptible to extreme climate phenomena, such as intense rainfall, flooding, and droughts, due to the influence of anomalous monsoons and complex terrain conditions. Consequently, a comprehensive examination of the spatiotemporal variation of PE in Guangdong Province and its connection to extreme events is of utmost importance. However, to the best of our knowledge, there is currently a dearth of related research.

Zhu *et al. Satellite Navigation*   (2024) 5:1

Page 3 of 17

Therefore, this study aims to calculate a high-resolution historical record of PE in Guangdong by utilizing a dense network of GNSS stations combined with precipitation products. Furthermore, it aims to analyze the characteristics of extreme drought and wetness events in conjunction with corresponding climate indices. The objectives of this study are as follows: (1) To investigate the spatial and temporal distribution and evolution of PE in Guangdong. (2) To characterize extreme climate events, both extreme drought and wetness, in Guangdong using longterm PE data. (3) To explore the frequency of dry and wet periods across multiple time scales in Guangdong. (4) To analyze the propagation relationship from meteorological anomalies to agricultural and hydrological anomalies in Guangdong.

Study area and data
Study area
The Guangdong province features a complex terrain with a higher altitude in the northeast and lower altitude in the southwest, predominantly dominated by hills and mountains, which constitute over 60% of the total area. The province can be roughly divided into three sub-regions

based on its terrain (Fig. 1): the northern part, consisting mainly of mountains and hills; the central part, comprising the Pearl River Delta, which is a low-lying impact plain, and the southern part, characterized by plains and terraces. Furthermore, Guangdong Province is characterized by a distinctive subtropical and tropical monsoon climate. The region exhibits an annual average temperature ranging from 15 to 25 degrees Celsius, accompanied by an average total annual precipitation of approximately 1500–2000 mm (He et al., 2017). Influenced by the summer monsoon and complex topography, precipitation is unevenly distributed throughout the year. Precipitation gradually increases from south to north and is concentrated mostly in the period from April to September, resulting in distinct rainy and dry seasons. Abundant precipitation in spring and summer makes the region susceptible to flood disasters, while the lower precipitation in autumn and winter can lead to drought events. In this study, we utilize multi-source hydrometeorological data to analyze the characteristics of extreme hydroclimate events in Guangdong. The objective is to mitigate the impact of such events and alleviate the pressure on water resources.
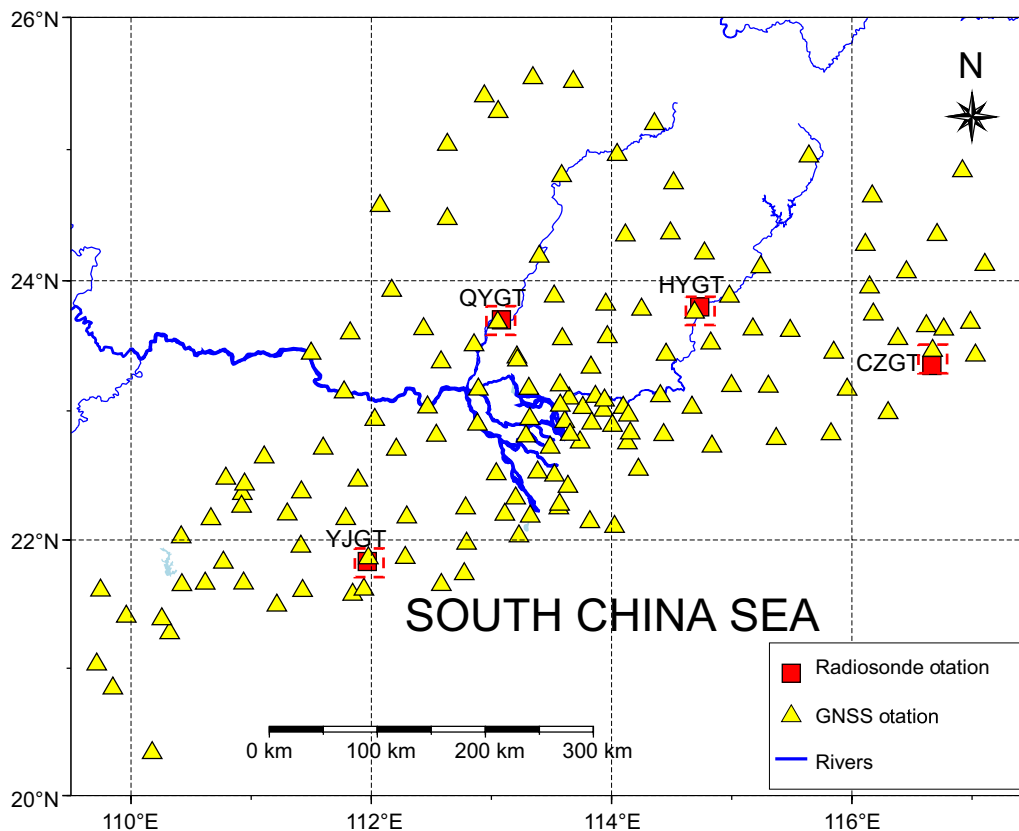

Fig. 1 The geographical location and station distribution of Guangdong. The GNSS stations are denoted by yellow triangles and radiosonde stations are represented by red squares. The red dashed box highlights the nearest GNSS station to the sounding station, providing convenient data comparison. The blue line denotes the river, while the red line marks the Pearl River Delta. Additionally, the background color illustrates the altitude

Zhu *et al. Satellite Navigation*   (2024) 5:1

Page 4 of 17

Data

In this study, we employed five types of data (Table 1), including GNSS data, reanalysis products, radiosonde data, hydrological models, and grid-based drought index products. Specifically, GNSS data were utilized to calculate the zenith tropospheric delay, which was subsequently converted to Precipitable Water Vapor (PWV). Hydrometeorological variables, such as temperature, precipitation, runoff, and soil moisture, and others, were derived for climate analysis using reanalysis products from the European Centre for Medium-Range Weather Forecasts (ECMWF) and hydrological models from the Global Land Data Assimilation System (GLDAS). Additionally, the grid-based drought index product was employed to assess the reliability of the related climate indices utilized in this investigation.

Detailed data descriptions are presented in the following paragraphs

GNSS data

The Lands and Resource Department of Guangdong, and the Crustal Movement Observation Network of China (CMONOC) have established a dense network of GNSS stations in Guangdong Province, which offers favorable conditions for investigating and analyzing extreme drought and wetness events. We obtained the observation data from 140 GNSS stations located throughout Guangdong province (see Table S1 for details), covering the period from January 1, 2007, to May 31, 2022. The spatial distribution of these stations is depicted in Fig. 1, which highlights their comprehensive coverage across most regions of Guangdong province, particularly the Guangdong-Hong Kong-Macao Greater Bay Area.

ECMWF reanalysis data

The ERA5 dataset, the latest reanalysis product from the ECMWF, offers very precise and high-resolution ground meteorological data spanning from 1940 to the present day, with continuous updates and extensions (Hersbach et al., 2020). This study utilized monthly averaged data on single levels, including 2 m temperature, surface pressure, total precipitation, runoff, and total column water vapor,

from January 2007 to May 2022. The data have a spatial resolution of 1/4° and a temporal resolution of 1 month. In this study, we utilize 2 m temperature and surface pressure data to compute the weighted mean temperature and zenith hydrostatic delay, which are essential parameters for the accurate determination of GNSS-derived PWV. Total precipitation data is combined with GNSS-derived PWV data to determine PE. Runoff data is employed to investigate the propagation relationship between meteorological anomalies and hydrological anomalies. In addition, to interpolate grid data to GNSS station positions, bilinear interpolation is utilized.

Radiosonde data

At radiosonde stations, sounding balloons are released every 12 h (UTC 0:00 12:00) to directly measure meteorological parameters, including temperature, pressure, and relative humidity, at different altitudes. By integrating these measurements over the profile, it is possible to calculate atmospheric precipitable water vapor. We utilized stratified meteorological data from the Integrated Global Radiosonde Archive Version 2 (IGRA2) to compute PWV as a supplementary method for validation in this study (Durre et al., 2016). Regrettably, our examination of the data set revealed only four observation records from radiosonde stations in Guangdong that match the study area and time of this paper (see Table S2 for details). Nevertheless, these stations are in diverse terrains and geographical locations across Guangdong, providing ample cross-validation between datasets. To mitigate the effects of distance and altitude, we compare and analyze the consistency between the PWV provided by GNSS and RS by selecting the four GNSS stations closest to the sounding station.

GLDAS hydrological model

The GLDAS hydrological model utilizes advanced land surface modeling and data assimilation techniques to assimilate satellite- and ground-based observational data products, generating an optimal field of land surface states and fluxes (Rodell et al., 2004). This study investigates the influence of meteorological anomalies

Table 1 Summary of the dataset utilized in the study

Type	Spatial coverage	Temporal coverage (Resolution)	Variables
GNSS data	Stations	From 2007–01 to 2022–05 (Daily)	Precipitable water vapor
ECMWF reanalysis product	0.25°	From 2007–01 to 2022–05 (Monthly)	Temperature, pressure, precipitation, runoff, and total column water vapor
Radiosonde data	Stations	From 2007–01 to 2021–05 (12-hourly)	Precipitable water vapor
GLDAS hydrological model	0.25°	From 2007–01 to 2022–05 (Monthly)	0-2 m soil moisture
SPEI product	0.5°	From 2007–01 to 2022–05 (Monthly)	Drought index

Zhu *et al. Satellite Navigation*   (2024) 5:1

Page 5 of 17

on agricultural anomalies associated with soil moisture fluctuations, utilizing 0-2 m soil moisture data from the GLDAS-Noah2.1 hydrological model (hereafter referred to as GLDAS). The dataset, provided by the National Aeronautics and Space Administration's Goddard Space Flight Center, offers a spatial resolution of 1/4° and a temporal resolution of 1 month.

SPEI drought index data

The Standardized Precipitation-Evapotranspiration Index (SPEI) is a comprehensive drought index that assesses drought conditions across multiple timescales (Vicente-Serrano et al., 2010). It is derived from the difference between precipitation and potential evapotranspiration, which is a key indicator of water availability in the climate water balance. The SPEIbase, a global SPEI database, offers dependable and long-term information on drought conditions at a 1/2° spatial and monthly temporal resolution (Beguería et al., 2010). In this study, the SPEI time series derived from SPEIbase was employed to assess the reliability of the drought index utilized.

Methodology

GNSS data processing

In the present study, we utilized the Precise Point Positioning (PPP) mode of the PANDA (Positioning And Navigation Data Analyst) software to accurately estimate the daily Zenith Tropospheric Delay (ZTD) (Shi et al., 2008). The Center for Orbit Determination in Europe (CODE) provided precise orbit, clock offset, and differential code bias files. The a priori values for the tropospheric delay were estimated using the Global Mapping Function (GMF) and the Global Pressure–Temperature (GPT) model. To correct for the first-order ionospheric effect, an ionosphere-free combination model was used. Additionally, the phase center of the antenna was corrected using the IGS antenna phase calibration model. Given the study's exclusive focus on sub-seasonal extreme drought and wetness events, we converted the daily ZTD time series, derived from GNSS, into monthly mean series to facilitate the relevant analysis (Fig. 2). Furthermore, the ZTD time series obtained by GNSS are often incomplete due to instrument failure or poor observation conditions. To address this issue, we utilized the Singular Spectrum Analysis (SSA) method to fill the gaps in the monthly mean time series. This non-parametric and data-adaptive approach produces reliable outcomes for gap filling (Yi & Sneeuw, 2021). To ensure the temporal integrity and spatial uniformity of station distribution, the extensive data gaps in the GNSS-derived precipitable water vapor time series, caused by the factors such as delayed construction of certain stations, are filled using the precipitable water vapor data from the ERA5 dataset.

Calculation of precipitable water vapor using multiple data
Estimating precipitable water vapor with GNSS observations

Precipitable water vapor is defined as the total water vapor content per unit area of the air column extending
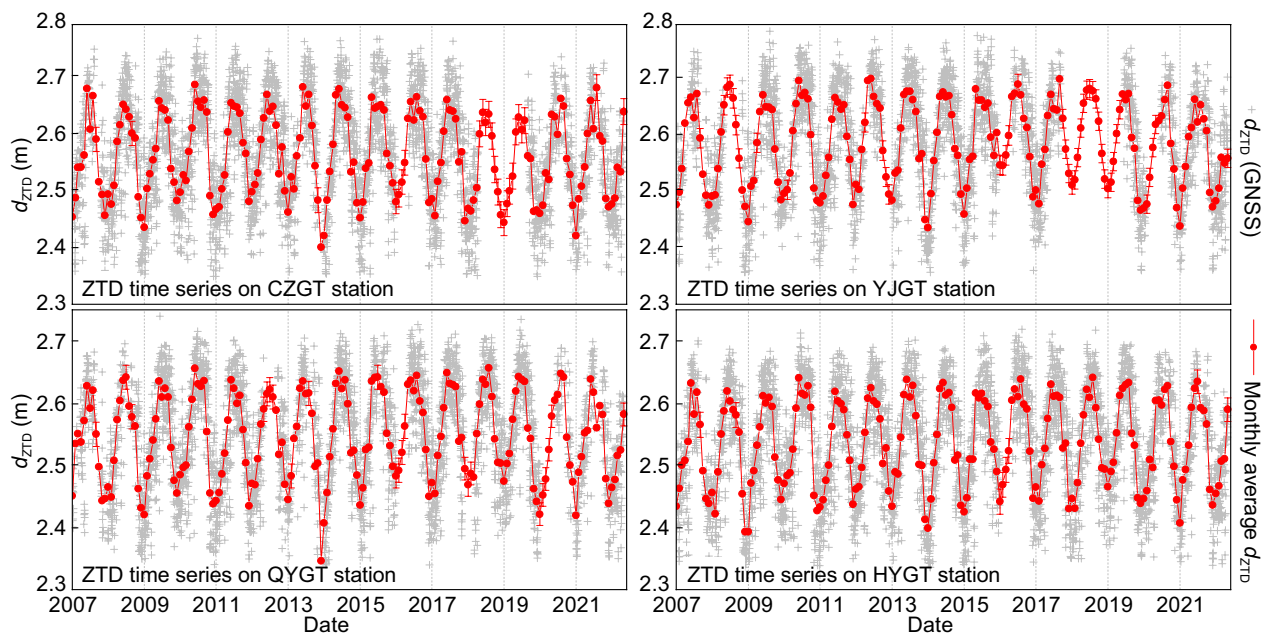

Fig. 2 The daily Zenith Tropospheric Delay (ZTD) time series and monthly mean series were obtained from four selected Global Navigation Satellite System (GNSS) stations, with the names of the stations displayed in the lower left corner of each subplot

Zhu *et al. Satellite Navigation*   (2024) 5:1

Page 6 of 17

from the Earth's surface to the top of the troposphere (Bevis et al., 1994). GNSS technique can determine accurate ZTD, which can subsequently be transformed into PWV using Eq. 1.

$$d_{\mathrm{PWV}} = d_{\mathrm{ZWD}} \times \Pi \tag{1}$$

In Eq. (1), d_{ZWD} represents the zenith wet delay, and Π denotes the dimensionless conversion factor, both of which can be obtained using Eqs. (2) and (3), respectively.

$$d_{\mathrm{ZWD}} = d_{\mathrm{ZTD}} - d_{\mathrm{ZHD}} d_{\mathrm{ZHD}} = \frac{0.0022768 \times P}{1 - 0.0026 \times \cos(\phi) - 0.00028 \times E} \tag{2}$$

In Eq. 2, d_{ZHD} represents the zenith hydrostatic delay, P denotes the surface air pressure, ϕ represents the latitude of the station, and E signifies the height of the station.

$$\Pi = \frac{1 \times 10^6}{\rho_w R_v (\frac{k_3}{T_m} + k_2\prime)} \tag{3}$$

Equation 3 incorporates several constants, including water density (ρ_w), the specific gas constant of water vapor (R_v), and atmospheric refractivity constants ($k_2\prime$ and k_3) (X. Wang et al., 2016a, 2016b, 2016c). The variable T_m denotes the weighted mean temperature, as estimated by the Bevis model (Bevis et al., 1992):

$$T_m = 0.72 \times T_s + 70.2 \tag{4}$$

In Eq. 4, T_s denotes the surface temperature, provided by the ERA5 dataset.

Estimating precipitable water vapor with radiosonde observations

Radiosonde stations record the various atmospheric parameters layer by layer, including, but not limited to, temperature, humidity, air pressure, wind direction, and wind velocity. To derive precipitable water vapor with radiosonde data, a numerical integration is necessary (Eq. 5).

$$d_{\mathrm{PWV}} = \frac{1}{g\rho} \sum_{p}^{p_0} q dp \tag{5}$$

Among these variables, g denotes the gravity, ρ is the density of liquid water, p denotes surface atmospheric pressure, p_0 signifies air pressure at the top of the atmosphere, and q represents the specific humidity (Eq. 6).

$$\begin{cases} q = \frac{0.622 \times P_w}{P - 0.378 \times P_w} \\ P_w = \frac{d_{\mathrm{RH}} P_s}{100} \\ P_s = 6.112 \times exp \left[\frac{17.67 \times (T - 273.15)}{T - 29.65} \right] \end{cases} \tag{6}$$

Herein, P_w denotes the partial pressure of water vapor, d_{RH} represents the relative humidity, P_s signifies the saturation water vapor pressure, and T indicates the temperature.

Principal component analysis

Principal Component Analysis (PCA) is a widely used method for transforming a set of potentially correlated variables into a set of independent variables via an orthogonal transformation (Abdi & Williams, 2010). The resulting variables are referred to as Principal Components (PCs), which represent the temporal basis functions of the data. The eigenvector matrix corresponds to the spatial patterns of the data, also known as spatial responses. By sorting the eigenvectors' variance contribution rates in descending order, one can identify the proportion of the original signal that each PC contributes. Typically, the first few PCs capture most of the variance in the original data, thereby preserving most of the information. PCA was employed to investigate the temporal trends and spatial distribution patterns of the data set $\widetilde{X}_{m \times n}$, where m represents the data length and n denotes the number of stations. This analysis was accomplished via singular value decomposition, and is represented mathematically by Eq. (7) (Ming et al., 2017).

$$\widetilde{X} = \boldsymbol{U} \times \boldsymbol{S} \times \boldsymbol{V}^{\mathrm{T}} \tag{7}$$

Here, $\boldsymbol{U}$ and $\boldsymbol{V}$ denote the temporal and spatial pattern matrices of $\widetilde{X}$, respectively, while $\boldsymbol{S}$ denotes the diagonal matrix of eigenvalues. Here, we provide a concise introduction to the principle of the PCA technique. For a more comprehensive understanding, refer to Abdi et al. (2010).

Precipitation efficiency

Precipitation efficiency denotes the fraction of average precipitable water vapor above a station that is effectively converted into measurable precipitation over a specific time interval. According to Bordi et al. (2015), PE can be quantified by computing the ratio between precipitation and atmospheric precipitable water vapor data, as illustrated in Eq. (8). Previous research has consistently demonstrated that higher PE values indicate a more efficient conversion of precipitation, resulting in wetter regions. Conversely, the areas with lower PE values tend to experience drier conditions (e.g., Ma et al., 2021; Zhu, Chen, Hu, Liu, et al., 2023).

$$d_{\mathrm{PE}} = \frac{P}{d_{\overline{\mathrm{PWV}}}} \times 100 \tag{8}$$

In Eq. 8, d_{PE} represents the precipitation efficiency (in percentage), the variable P denotes the monthly average precipitation, and $d_{\overline{PWV}}$ signifies the monthly average of PWV.

Climate index

The climate index condenses intricate drought or wet occurrences into a single numeric value (e.g., McKee et al., 1993; Yao et al., 2022; Zhu, Chen, Hu, Wei, et al., 2023a, 2023b). This is achieved through the application of a principle that involves computing the likelihood of such extreme weather phenomena based on historical observations of relevant hydrometeorological variables, and subsequently converting this probability into a corresponding index, which represents the potential for these events. In this study, we utilize the Standardized Precipitation Conversion Index (SPCI) to detect meteorological anomalies (Zhao et al., 2020a, 2020b). The SPCI, a meteorological drought index that accounts for the intensity and duration of droughts, is calculated using historical records of PE. As a standardized metric, the SPCI can also serve as an indicator of wet periods.

$$d_{SPCI}^n = \mathrm{nor}\left[\left(\frac{\sum_{i=m}^{m+n-1} d_{\overline{P}}^i}{\sum_{i=m}^{m+n-1} d_{\overline{PWV}}^i \times d_{day}^i} \times 100 \right)_n \right] \quad (9)$$

In Eq. 9, i represents the month, m represents the first month of the multi-month scale, n represents the total number of months on the scale, $d_{\overline{P}}^i$ represents the average precipitation in the i-th month, $d_{\overline{PWV}}^i$ represents the average PWV in the i-th month, and d_{day}^i represents the number of days in the i-th month. The "nor" refers to normalization.

As SPCI values increase, the precipitation conversion rate and regional wetness also increase, indicating wetter conditions, whereas smaller SPCI values suggest drier conditions. In this study, the empirical Cumulative Distribution Function (eCDF) was utilized to compute the statistical percentiles of SPCI1. The upper and lower quantiles of SPCI1 in Guangdong were approximately 0.46 and − 0.41, respectively. As the original drought/wet classification catalog of SPCI (Table S3) may not account for all meteorological and hydrological events, it was not employed in this study. Instead, Table 2 presents the drought/wet classification catalog used herein. Specifically, when SPCI exceeds 0.5, the likelihood of extreme wetness increases with higher SPCI values, while the probability of drought increases with decreasing SPCI below − 0.5.

While the SPCI can provide valuable insights into atypical shifts in precipitation efficiency, it is crucial

Table 2 The drought/wet classification catalog

Category	Range	Level
W4	[2, +∞]	Exceptionally wet
W3	[1.6, 1.99]	Extremely wet
W2	[1.3, 1.59]	Severe wet
W1	[0.8, 1.29]	Moderately wet
W0	[0.5, 0.79]	Slight wet
WD	[−0.49, 0.49]	Near normal
D0	[−0.79, −0.5]	Abnormal drought
D1	[−1.29, −0.8]	Moderate drought
D2	[−1.59, −1.3]	Severe drought
D3	[−1.99, −1.6]	Extremely drought
D4	(−∞, −2]	Exceptional drought

to acknowledge that these precipitation anomalies can potentially trigger irregularities in both soil moisture and runoff, particularly within the framework of extreme event development. In this research, we have leveraged the Standardized Soil Moisture Index (SSMI) and the Standardized Runoff Index (SRI) to pinpoint agricultural and hydrological anomalies, respectively. Our primary objective has been to assess the impact of meteorological anomalies on agricultural and hydrological systems. Notably, both indices can be readily computed using Eq. 10.

$$d_{CI}^{i,j} = \frac{W_{i,j} - \overline{W}_j}{\sigma_j} \quad (10)$$

In Eq. (10), $d_{CI}^{i,j}$ represents the climate index, denoted as either SSMI or SRI. The variables i and j are the year (2007–2022) and month (1–12), respectively. $W_{i,j}$ is the soil moisture or runoff of the jth month of the ith year. $\overline{W}_j$ represents monthly climatology, which is the average soil moisture or runoff of j months for all years. σ_j is the standard deviation of j months for all years.

Propagation relationship

Pearson's Correlation Coefficient (PCC) is widely used for quantifying the linear relationship between two random variables (Sedgwick, 2012). The PCC is a normalized measure of covariance that is calculated as the ratio of the product of the covariance to the standard deviation of the two variables (Eq. 11). A PCC value greater than 0 indicates a positive correlation, while a value less than 0 indicates a negative correlation; a value of 0 indicates no correlation. In this study, we employ PCC to assess the consistency between time series of various hydrometeorological variables.

$$d_{\mathrm{PCC}} = \frac{\mathrm{Cov}(X,Y)}{\sigma(X)\sigma(Y)} = \frac{\sum(x_i - \mu_x)(y_i - \mu_y)}{\sqrt{\sum(x_i - \mu_x)^2}\sqrt{\sum(y_i - \mu_y)^2}} \tag{11}$$

In Eq. 11, $\mathrm{Cov}(X,Y)$ represents covariance, $\sigma(x)$ and $\sigma(y)$ denote standard deviation of x_i and y_i, respectively, and μ_x and μ_y denote the respective mean values of x_i and y_i.

Furthermore, previous studies employed the Maximum Pearson Correlation Coefficient (MPCC) as a metric to determine the Propagation Time (PT) between meteorological, agricultural, and hydrological anomalies (e.g., Dai et al., 2022; Ding et al., 2021). Specifically, the MPCC is utilized to evaluate the PT between the accumulation period of the Meteorological Drought Index (MDI), denoted as MDI-n (where n signifies the number of months), and the Agricultural and Hydrological Drought Index for a single month (ADI-1/HDI-1). Consequently, this study employs the MPCC to determine the PT from meteorological to agricultural and hydrological anomalies. Following the determination of PT, we employed continuous wavelet transform to analyze the periodicity of meteorological and hydrological anomalies, facilitating a better understanding of their interrelationship (Q. Li et al., 2020a, 2020b). Wavelet transform is a commonly utilized time–frequency analysis tool in the field of hydrology and climate, enabling the decomposition of time series into the time and frequency domains simultaneously for signal characteristic extraction. The wavelet decomposition of a time series $X_n (n = 1, 2 \ldots N)$ can be implemented using Eq. (12).

$$W_n(s) = \sum_{n'=0}^{N-1} x_{n'} \varphi^* \left[\frac{(n'-n)\delta t}{s} \right] \tag{12}$$

In Eq. 12, the wavelet power spectrum is defined as $|W_n(s)|^2$, n is the localized time index, n' is the time conversion index, $\varphi(t)$ denotes a mother wavelet function, $(*)$ indicates the complex conjugate, s is the scale, and δt represents the sampling period. The wavelet power spectrum reflects the volatility characteristics of different scales present in the time series, with intensity changes observed at varying scales (Zhou, Shi, Fu, Ding, Li, Wang, et al., 2021).

Results

Temporal and spatial variations in precipitation efficiency in Guangdong

As mentioned previously, PE reflects a region's actual precipitation conversion rate and is a crucial indicator for evaluating its drought or wet (Bordi et al., 2014). Therefore, analyzing the spatiotemporal characteristics of PE in Guangdong is necessary to identify the areas susceptible to meteorological anomalies and provide insights for implementing appropriate disaster prevention and mitigation measures. By conducting PCA analysis on PE data at GNSS stations, we found that the first three principal components accounted for 92.87% of the cumulative variance of PEs in Guangdong, China, effectively describing the spatiotemporal distribution of PEs. Based on the time response of the first principal component of PE (with a variance contribution rate of 76.89%), it is evident that PE in Guangdong exhibits a pronounced seasonal
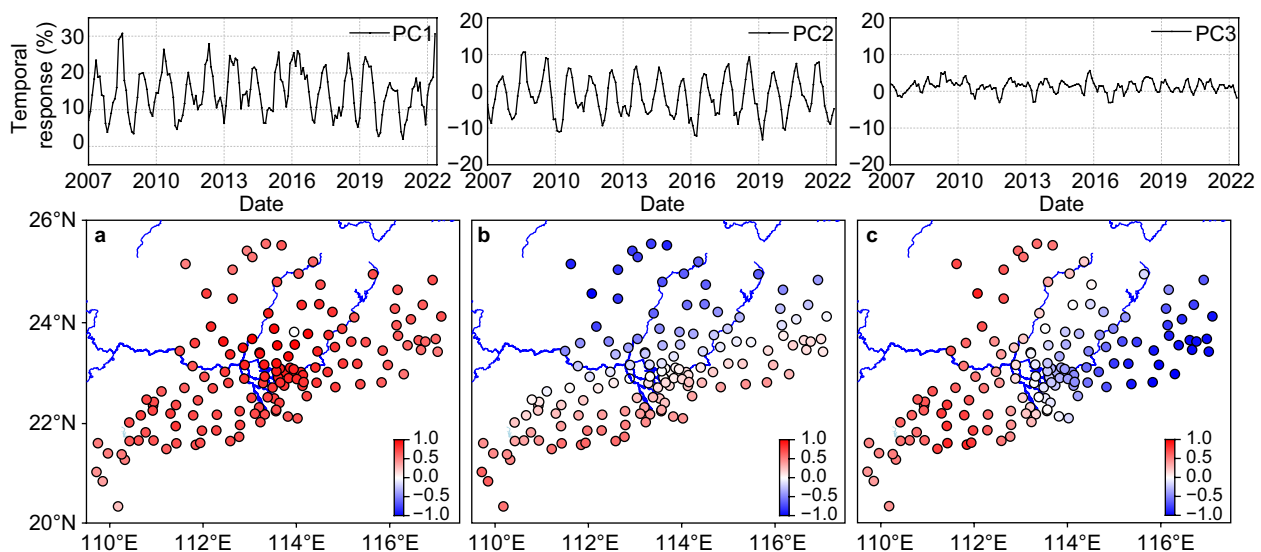

Fig. 3 Temporal and spatial responses of the first three principal components of precipitation efficiency

trend, with an unimodal distribution throughout the year (Fig. 3a). This implies that precipitation in Guangdong is unevenly distributed across the year, with distinct dry (October–March) and rainy seasons (April-September). The spatial response of the first principal component is consistent, with a high-value area near the Pearl River Delta plain that gradually decreases towards the east and west. This indicates that PE changes more dramatically in this region, leading to a higher risk of drought or flood disasters. The second principal component of PE contributed 12.03% to the variance, indicating a secondary distribution of PE (Fig. 3b). The temporal response of PC2 is positive from May to October and negative from November to April, and the spatial response exhibits an obvious north–south inverse pattern, highlighting the heterogeneous distribution of PE between the southern and northern regions of Guangdong. Additionally, a contrasting trend of increasing or decreasing PE is observed between the two regions. The third principal component of PE contributes only 3.95% to the total variance and has little impact on the original time series (Fig. 3c). Its spatiotemporal response indicates the presence of small-scale differences in PE between eastern and western Guangdong.

Detection of extreme drought and wetness events through anomalies in precipitation efficiency

In China, Guangdong is frequently affected by hydrometeorological disasters, with droughts and floods occurring periodically. Through the calculation of PE and its anomalies, our study reveals that PE in Guangdong exhibits an annual fluctuation ranging between 5%-25% (Fig. 4a), reaching its peak from April to September during the rainy season and hitting the lowest point from October to March during the dry season. Additionally, the magnitude of PE anomalies is typically within 10%, with its peak and trough values often corresponding to extreme wetness or dryness conditions (Fig. 4b). We converted the PE anomaly into a climate index (SPCI) to accurately reflect the meteorological anomaly resulting from the increase or decrease of PE in a clear and intuitive manner (Fig. 4c). Unlike the SPI, which relies solely on precipitation anomalies to gauge meteorological drought, the SPCI accounts for the influence of dynamic mechanisms on atmospheric moisture release, allowing for the comprehensive assessment of PE deficits across various time scales. In this study, we employ the 1-month scale SPCI (SPCI1) to detect potential extreme drought and wetness events in Guangdong, providing an early warning of anomalous precipitation conversion rates and aiding
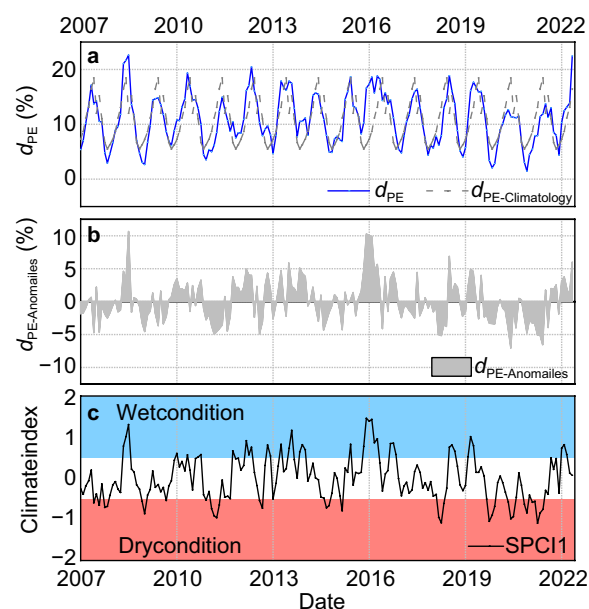

Fig. 4 The time series of precipitation efficiency in Guangdong and its corresponding climatology (**a**), along with the precipitation efficiency anomaly (**b**) and the standard precipitation conversion index calculated by precipitation efficiency (**c**). To reduce noise, a 3-month mean filtering is applied

in the evaluation of their severity. In accordance with the definition of drought by Thomas et al. (2014), we define an extreme climate event, encompassing both extreme wet and drought conditions, as persistent abnormal PE lasting for over three consecutive months. Consequently, each event has a defined duration from its inception to its conclusion, and intensity for each month that the event continues.

Table 3 provides a summary of the observed extreme drought and wetness events in Guangdong. Between January 2007 and May 2022, Guangdong experienced nine extreme wet events lasting for three to six months. Among these events, the severe wet (W2) event in November 2015, which lasted for six months and had a SPCI1 peak of 1.45 in December 2015. This rare heavy rainfall event in winter is believed to be triggered by the El Niño event, which peaked in November–December 2015, causing a substantial increase in precipitation in southeastern China (Zhai et al., 2016). Due to its proximity to the South China Sea and frequent exposure to typhoons that carry substantial amounts of water vapor, Guangdong experiences heavy precipitation during these extreme weather events. Among the nine extreme wet events we documented, the majority is linked to typhoon occurrences, as previously reported in other studies (e.g.,

Table 3 Extremely wet/dry events in Guangdong

Extremely wet events				Extremely dry events			
Num	Start time-End time	Duration in months	Highest severity (SPCI/Catalog)	Num	Start time-End time	Duration in months	Highest severity (SPCI/Catalog)
1	From 2008–05 to 2008–07	3	1.31/W2	1	From 2011–02 to 2011–05	4	− 0.95/D1
2	From 2012–03 to 2012–05	3	0.92/W1	2	From 2014–08 to 2011–10	3	− 0.71/D0
3	From 2013–07 to 2013–09	3	1.16/W1	3	From 2018–03 to 2018–05	3	− 1.08/D1
4	From 2013–11 to 2014–01	3	0.82/W1	4	From 2019–09 to 2019–12	4	− 1.04/D1
5	From 2015–11 to 2016–04	6	1.45/W2	5	From 2020–05 to 2020–07	3	− 0.98/D1
6	From 2016–09 to 2016–11	3	0.85/W1	6	From 2021–02 to 2021–06	5	− 1.09/D1
7	From 2018–07 to 2018–09	3	0.81/W1				
8	From 2019–02 to 2019–04	3	1.00/W1				
9	From 2022–01 to 2022–03	3	0.81/W1				

D. Wang et al., 2016a, 2016b, 2016c; H. Li et al., 2020a, 2020b). Furthermore, this study included monitoring six extreme drought events, lasting for 3 to 5 months each. Despite Guangdong's tropical and subtropical monsoon climate that receives abundant rainfall, the region faces the persistent risk of water shortages due to uneven temporal and spatial precipitation patterns, coupled with high temperatures and significant evaporation (C. Liu et al., 2011). As a result, drought remains a critical disaster that demands attention and action in Guangdong.

Investigating the wet and dry frequency at multiple time scales

The wet and dry frequency is a crucial determinant for assessing the likelihood of extremely dry or wet events. The areas characterized by higher frequencies are at greater risk of experiencing anomalies in the form of wet or dry conditions in the future. To facilitate comprehension, this paper defines the frequency of dry or wet as the ratio of the number of dry (SPCI < -0.5) or wet (SPCI > 0.5) months to the total number of months. Moreover, the SPCI is able to quantify PE anomalies
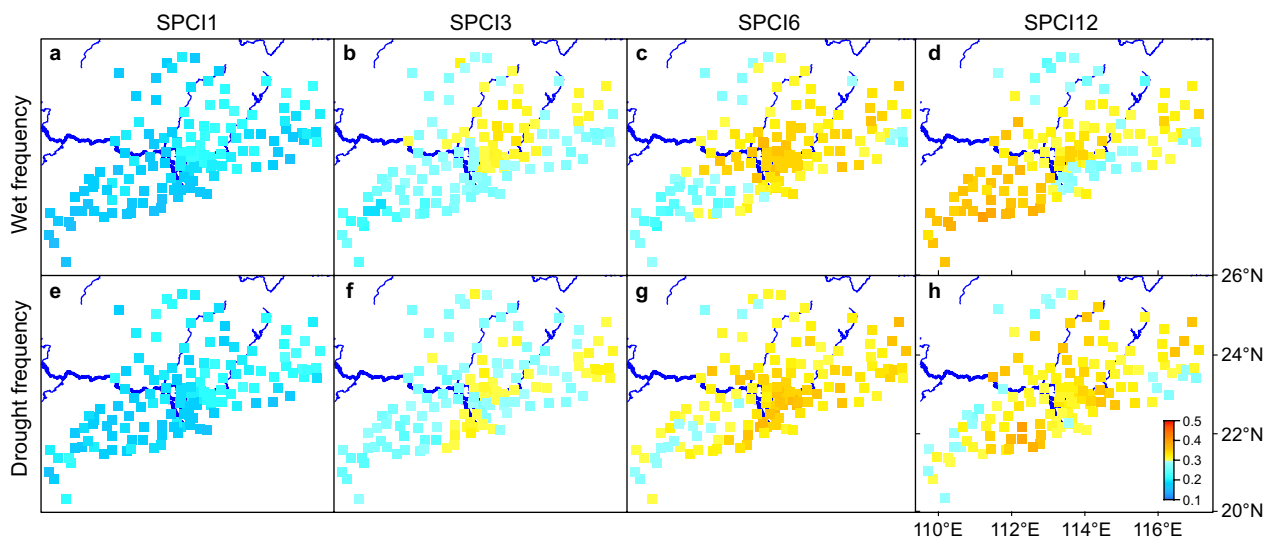

Fig. 5 The spatial distribution of wet and dry frequencies at various time scales. Wet frequencies (1-, 3-, 6-, 12-month scale SPCI) are presented in panels (**a**–**d**), while dry frequencies (1-, 3-, 6-, 12-month scale SPCI) are displayed in panels (**e**–**h**). SPCI: Standardized Precipitation Conversion Index

across various temporal scales, thereby providing insight into the impact of PE deficits on the availability of diverse water resources (Zhao et al., 2020a, 2020b). For instance, the anomalies in PE over shorter timescales (1–6 months) can induce alterations in meteorological and soil moisture conditions impacting agriculture. Conversely, the anomalies spanning longer timescales (6–12 months) can exert considerable influence on river runoff, reservoir storage, and groundwater storage, thereby affecting hydrological processes. To this end, we calculated the dry and wet frequencies of SPCI on 1-, 3-, 6-, and 12-month scales (Fig. 5). Due to the limited sample size of approximately 15.4 years, we did not analyze the indices on longer time scales.

According to the findings of this study, significant spatial variations are observed in the wet and dry frequencies across different time scales. Moreover, as the time scale increases (i.e., 1–12 months), both wet and dry frequencies exhibit a gradual increase. Notably, the analysis reveals a distinct southwest-northeast difference in the spatial distribution of the dry and wet frequencies for SPCI1, suggesting that the northeast region may be more susceptible to extremely dry and wet events. Additionally, the high-value areas of dry–wet frequency for SPCI3 are primarily concentrated in the Pearl River Delta region. As an alluvial plain characterized by flat topography and intricate water systems, the Pearl River Delta region is highly vulnerable to short-term meteorological anomalies, which can have consequential impacts on agricultural systems. The distribution pattern of SPCI6 closely resembles that of SPCI3, suggesting a persistently high occurrence of mid-term meteorological anomalies in the Pearl River Delta region, potentially affecting the hydrological system. Moreover, the spatial distribution of wet frequency associated with SPCI12 demonstrates a southward trend, while the distribution of dry frequency

exhibits a northward trend, implying that different terrains may exhibit diverse responses to long-term meteorological anomalies. Overall, our study highlights the severity of the impacts of varying-scale meteorological anomalies on the Pearl River Delta region. The region's vulnerability to these anomalies, especially in terms of short-term and mid-term events, underscores the importance of developing appropriate strategies to mitigate potential agricultural and hydrological disruptions.

Investigating the propagation relationship between meteorological anomalies and agricultural as well as hydrological anomalies.

Following a meteorological anomaly, such as drought, its repercussions permeate the agriculture and hydrological system, leading to abnormal declines in soil moisture and river runoff (Van Loon, 2015). This inadequacy in soil moisture has a direct impact on vegetation growth and crop yields, which is commonly referred to as agricultural drought. Furthermore, it can diminish both surface and subsurface runoff, thereby significantly impacting the water supply, and further generating hydrological drought. This study employs the 1-month scale Standardized Soil Moisture Index (SSMI1) and Standardized Runoff Index (SRI1) to characterize agricultural and hydrological anomalies, respectively. Additionally, previous research has demonstrated the efficacy of using the MPCC between different climate indices to analyze the propagation relationship between different anomaly types, yielding satisfactory results (e.g., Wu et al., 2021; Zhou, Shi, Fu, Ding, Li, Wang, et al., 2021). We calculated the PCC between the 1–24 month-scale SPCI (SPCI1-24) and SSMI1 as well as SRI (Fig. 6a). Our results demonstrate a robust association between meteorological anomalies in Guangdong and agricultural and hydrological anomalies. Particularly, SPCI3 exhibits the highest PCC with SSMI1 and SRI1, with values of 0.81
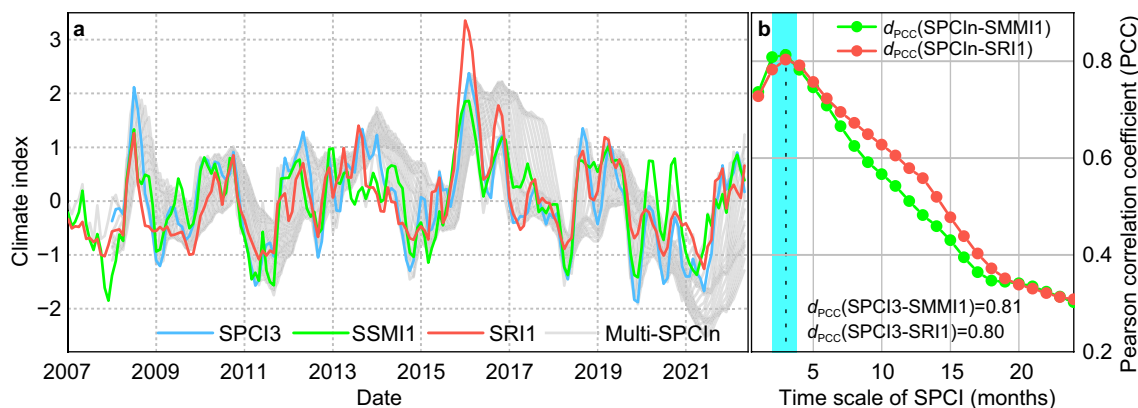

Fig. 6 SPCI1-24, SSMI1, and SRI1 time series in Guangdong (**a**), and the respective correlations between SPCIn and SSMI1, as well as SRI1 (**b**). SPCI: Standardized Precipitation Conversion Index; SSMI: Standardized Soil Moisture Index; SRI: Standardized Runoff Index
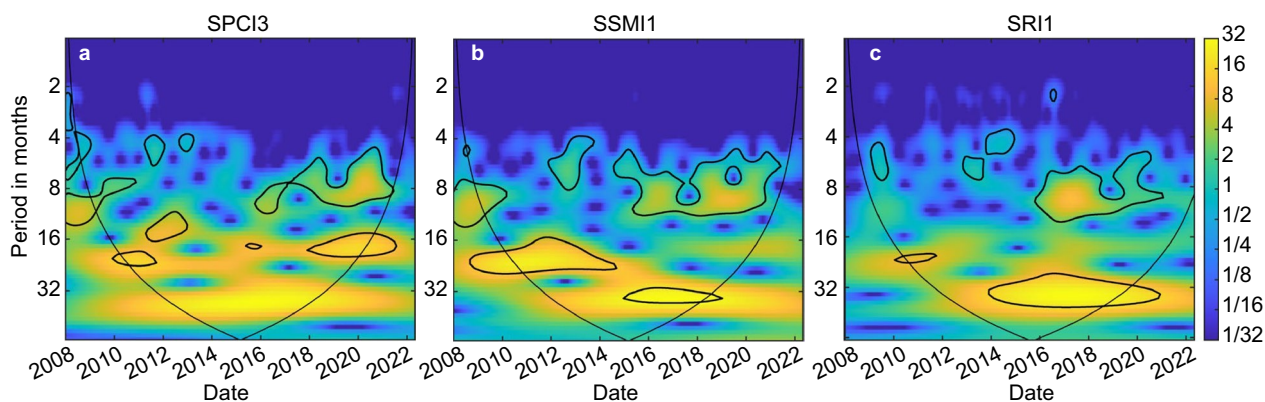
Zhu *et al. Satellite Navigation*   (2024) 5:1

Page 12 of 17

Fig. 7 Continuous wavelet power spectrum of the SPCI3 (**a**), SSMI1(**b**), and SRI1 (**c**) in Guangdong. The region within the black cone-shaped outline represents the area unaffected by edge effects, while the region outside the black cone-shaped outline denotes the area influenced by the cone of influence. A thick outline indicates a 95% confidence level of significance. The background colors correspond to wavelet energies

Table 4 Summary of the periodicities of SPCI3, SSMI1 and SRI1 in Guangdong

Num	SPCI3	SSMI1	SRI1
1	4–7 months (From 2008 to 2009)	7–14 months (From 2008 to 2010)	4–8 months (From 2009 to 2010)
2	7–14 months (From 2008 to 2011)	16–26 months (From 2009 to 2015)	20–22 months (From 2010 to 2012)
3	20–24 months (From 2010 to 2012)	4–8 months (From 2012 to 2014)	6–8 months (From 2013 to 2014)
4	4–6 months (From 2011 to 2012)	5–12 months (From 2014 to 2021)	4–5 months (From 2014 to 2015)
5	12–16 months (From 2011 to 2013)	32–40 months (From 2015 to 2019)	5–14 months (From 2016 to 2021)
6	5–12 months (From 2016 to 2021)		
7	16–20 months (From 2018 to 2021)		

and 0.80, respectively (Fig. 6b), indicating a propagation time of approximately three months from meteorological anomalies to agricultural and hydrological anomalies. This observation aligns with the conclusions drawn by Zhou et al., (2021a, 2021b).

This study presents the findings of a comprehensive analysis using continuous wavelet transform on SPCI3, SSMI1, and SRI1 datasets, with a confidence level of 95%. Figure 7 illustrates the corresponding wavelet power spectra, while Table 4 provides a detailed summary of the significant periodicities observed in Guangdong for SPCI3, SSMI1, and SRI1. The findings reveal distinct periodic patterns in SPCI3 across various periods, including 4 to 7, 7 to 14, 20 to 24, 4 to 6, 12 to 16, 5 to 12, and 16 to 20 months from 2008 to 2021 (Fig. 7a). Notably, the periodicity of SSMI1 and SRI1 closely resembles that of SPCI3. Specifically, SSMI1 displays significant periodic patterns spanning 7 to 14, 16 to 26, 4 to 8, 5 to 12, and 32 to 40 months from 2008 to 2019 (Fig. 7b). Similarly, SRI1 shows significant periodic patterns ranging from 4 to 8, 20 to 22, 6 to 8, 4 to 5, and 5 to 14 months from 2009 to 2021 (Fig. 7c). The correlation and periodicity characteristics between SPCI3 and SSMI1as well as SRI1 underscore the significant role played by the periodic nature of meteorological anomalies in driving patterns of agricultural and hydrological anomalies.

Discussion

A comparative analysis of precipitable water vapor datasets

We compiled the daily precipitable water vapor data obtained at four GNSS stations (GNSS-PWV) in a monthly mean series and analyzed it in conjunction with the PWV time series derived from RS (RS-PWV) and ERA5 (ERA5-PWV) datasets to evaluate their consistency (Fig. 8). Significantly, the scarcity of RS data records near the YJGT and HYGT GNSS stations is a critical limitation, resulting in our reliance on a limited dataset for the calculations (Fig. 8b, d). The study's findings demonstrated a robust positive correlation between GNSS-PWV and RS-PWV, as well as ERA5-PWV, consistently surpassing 0.95 (the detailed information provided in the lower left of Fig. 8). This highlights the high
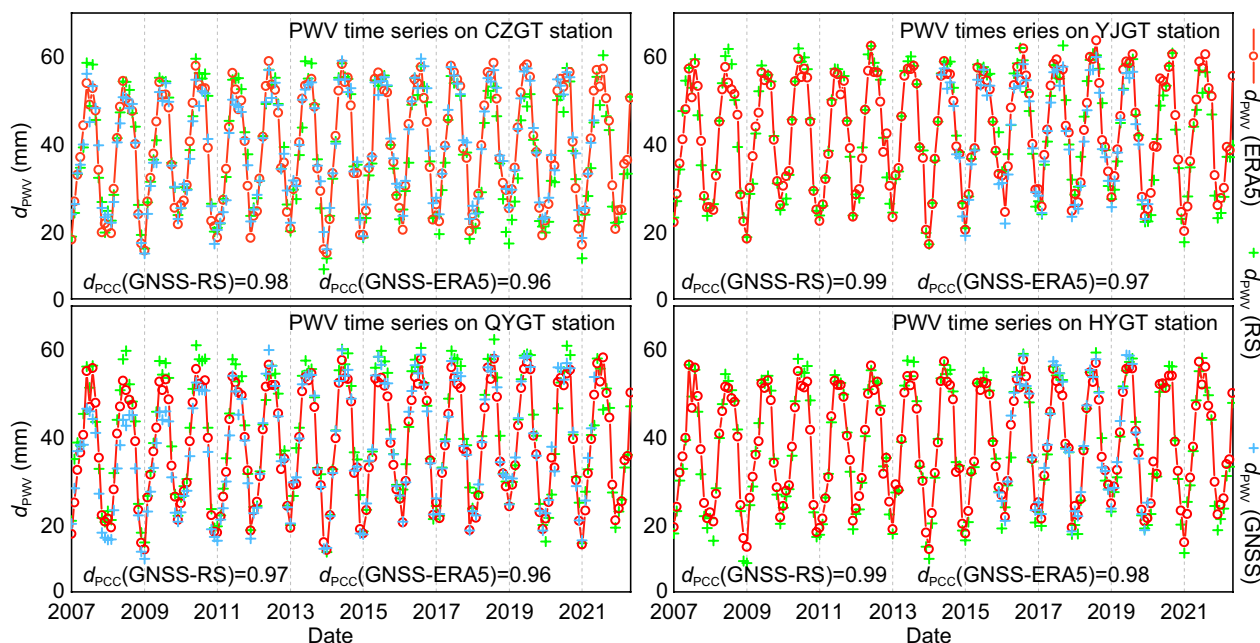
Fig. 8 Comparison of the PWV derived from GNSS, radiosonde stations (RS), and ERA5 datasets. The lower left corner of each subplot shows the Pearson correlation coefficients between GNSS and RS, as well as GNSS and ERA5

reliability of the GNSS-PWV employed in this investigation. Furthermore, RS has long been recognized as a dependable source of measured data, frequently employed as a reference to validate the accuracy of other datasets (e.g., Z. Gui et al., 2017; Li et al., 2003). To assess the rationality of utilizing ERA5 data for interpolating long-term gaps in the GNSS time series, we compared the PWV data derived with RS with the results derived with GNSS and ERA5 in this study. Evaluation indicators such as average deviation (bias) and Root Mean Square Error (RMSE) are employed to analyze the reliability and accuracy of GNSS and ERA5 data. The results demonstrate comparable accuracy between monthly GNSS-PWV and ERA5-PWV in Guangdong, with only minor discrepancies. Statistically, the GNSS-PWV reveals a bias of 0.24 mm and an RMSE of 2.62 mm, while the ERA5-PWV indicates a bias of 0.85 mm and an RMSE of 3.17 mm. Although the GNSS exhibits slightly better performance than the ERA5, the degree of difference is negligible when examining climate anomalies on long-term scales.

Comparison among multi-scale climate indices in Guangdong

Ensuring the accurate capture of extreme drought and wetness events and their characteristics is contingent upon the reliability of climate indices. To that end, we systematically compare the climate indices of varying scales (SPCI1, SPCI3, SPCI6, and SPCI12) employed in

this study with SPI and SPEI, respectively, at the same time scale (Fig. 9). We discover a remarkable correlation between the SPCI and both the SPI and the SPEI at various time scales in Guangdong. Moreover, as the time scale extended, the intensity of both wet and dry events, as indicated by all climate indices, is escalated. This finding strongly suggests that the SPCI utilized in this study exhibits accuracy and reliability in effectively capturing extreme drought and wetness events. Across all four time scales, the PCCs of the SPCI and SPI demonstrate a high degree of consistency, with respective values of 0.98, 0.97, 0.96, and 0.94. This outcome is expected, considering the significant contribution of precipitation to the estimation of PE. However, in essence, precipitation can be conceptualized as the flux of water vapor within a convective system; yet, it is important to note that not all water vapor flux contributes to precipitation (e.g., Sui et al., 2007; Tuller, 1971). Consequently, employing PE rather than pure precipitation is more suitable for detecting meteorological anomalies. In addition, the PCCs of SPCI and SPEI across the four time scales are found to be 0.82, 0.80, 0.79, and 0.76, respectively. While the time series of both indices exhibit a strong correlation, subtle divergences exist in certain local nuances, potentially attributed to temperature fluctuations. Previous studies have consistently demonstrated that increasing temperatures exert a notably amplified influence on the severity of droughts (e.g., Karl et al., 2012; Vicente-Serrano et al., 2014).
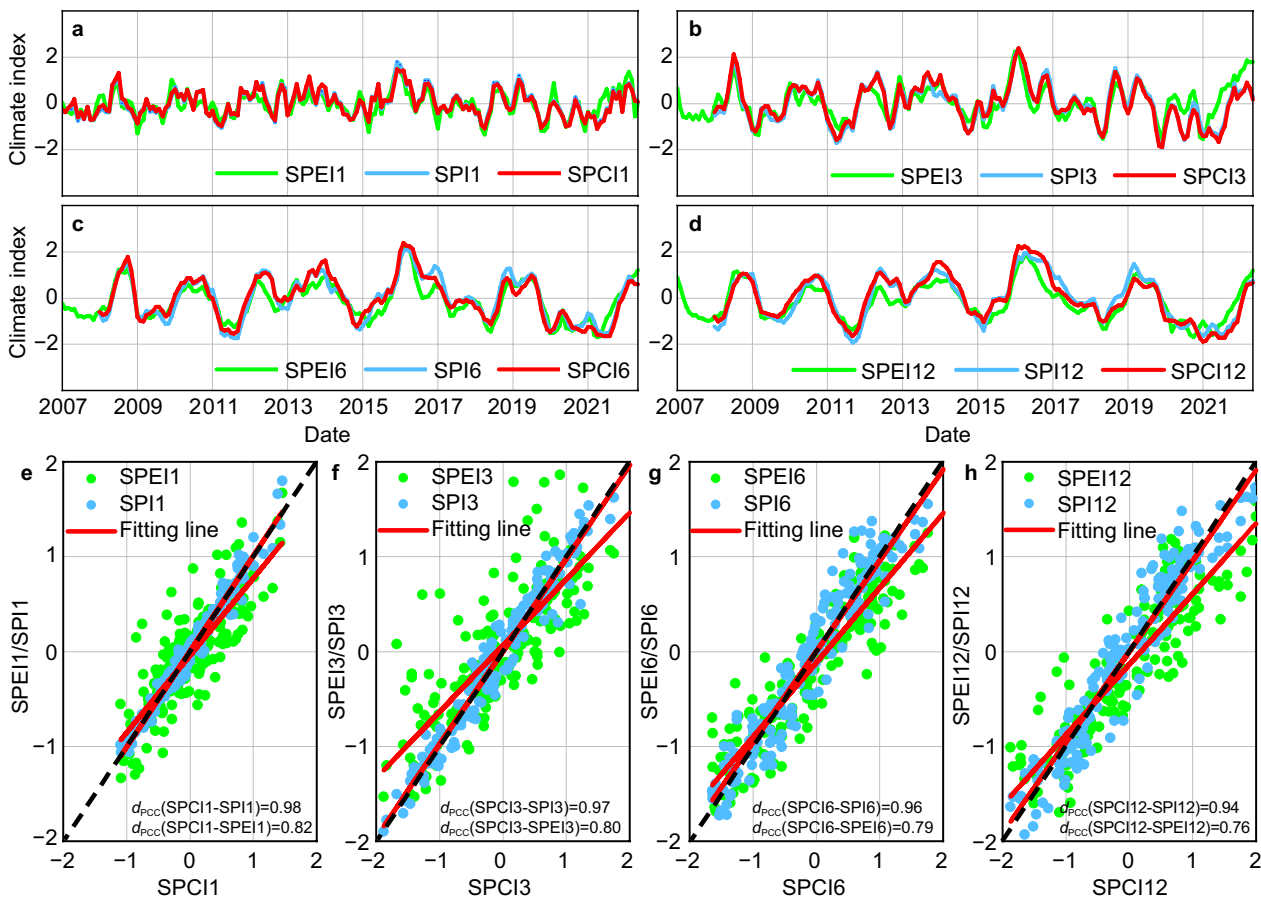
Fig. 9 Comparison of climate indices at different time scales, **a** 1-month, **b** 3-months, **c** 6-months, **d** 12-months. SPCI: Standardized Precipitation Conversion Index; SPI: Standardized Precipitation Index; SPEI: Standardized Precipitation-Evapotranspiration Index. Subfigures **e**–**h** depict the linear regression between SPCI and SPI, as well as SPEI, across various time scales

Limitations of this study

While this study provides a systematic analysis of extreme drought and wetness events and their characteristics in Guangdong, China, utilizing PE and its derived climate index, there are certain limitations to be acknowledged. Firstly, according to statistical reliability requirements, the historical PE records for over 30 years are recommended, whereas this paper employed a data time span of only 15.4 years. However, it is crucial to note that the primary objective of this research is to emphasize the applicability of GNSS for monitoring meteorological anomalies. With the accumulation of observation records, future studies will benefit from an expanded dataset. Secondly, it should be recognized that the findings of this study are much influenced by the substantial variability in the PE observed in Guangdong. As a result, substantial disparities in meteorological anomalies across diverse regions, such as notable fluctuations in temperature, evapotranspiration, and prolonged absence of precipitation, underscore the necessity for targeted analyses addressing distinct issues.

Conclusion

In this study, we utilized GNSS-derived precipitable water vapor data in Guangdong, combined with the precipitation data, to calculate the precipitation efficiency time series, and investigate historical extreme drought and wetness events and their characteristics in the region. Our analysis unveils a clear seasonal pattern in precipitation efficiency, ranging from 5 to 25%. The spatial distribution of precipitation efficiency exhibits discernible variations, with higher values in the Pearl River Delta region and gradually decreasing towards the eastern and western areas. By integrating precipitation efficiency anomalies with climate indices, we identified nine extreme wet events and six extreme drought events in Guangdong. Notably, we observed a rising trend in the wet and dry frequency with longer time scales. The Pearl River Delta region exhibited higher frequencies of extreme events, potentially attributed to its intricate topography. The correlation and wavelet analyses indicated a 3-month propagation time from meteorological

Zhu *et al. Satellite Navigation* (2024) 5:1

Page 15 of 17

anomalies to agricultural and hydrological anomalies in Guangdong. Moreover, we deduced that the occurrence of meteorological anomalies serves as the primary driver for the emergence of agricultural and hydrological anomalies. Rigorous validation of our GNSS-derived precipitable water vapor data and consistency checks of climate indices further ensured the reliability and accuracy of our findings. Overall, this study enhances our understanding of extreme drought and wetness events, aiding the development of effective strategies for disaster prevention and mitigation.

Supplementary Information

The online version contains supplementary material available at https://doi.org/10.1186/s43020-023-00121-6.

> **Supplementary Tables: Appendix.**

Author contributions
Hai Zhu contributed to the methodology and writing of the manuscript. Kejie Chen provided supervision, project administration, and funding acquisition, and conceived this study. Haishan Chai contributed to the review and editing process. Yuanbin Ye and Wenjian Liu played a key role in providing and curating the data. All authors have thoroughly reviewed and approved the final manuscript.

Data availability
The GNSS data used in this study were obtained from the China Earthquake Networks Center (https://data.earthquake.cn/) and the Lands and Resource Department of Guangdong Province. Gridded meteorological products were sourced from the European Centre for Medium-Range Weather Forecasts (https://www.ecmwf.int/). Radiosonde data were retrieved from the Integrated Global Radiosonde Archive Version 2 (https://www1.ncdc.noaa.gov/pub/data/igra/). The GLDAS-Noah2.1 hydrological model is accessible through the Goddard Earth Sciences Data and Information Services Center archive (GES DISC) (https://disc.gsfc.nasa.gov/). Standardized Precipitation-Evapotranspiration Index (SPEI) products were provided by the Global SPEI database (https://spei.csic.es/database.html). Certain figures were created using the Generic Mapping Tools (version 6.0.0) software (Wessel et al., 2019).

Declarations

Competing interests
The authors declare that they have no known competing financial interests or personal relationships that could have influenced the work reported in this study.

References
Abdi, H., & Williams, L. J. (2010). Principal component analysis. *Wiley Interdisciplinary Reviews: Computational Statistics, 2*, 433–459. https://doi.org/10.1002/wics.101

Beguería, S., Vicente-Serrano, S. M., & Angulo-Martínez, M. (2010). A multiscalar global drought dataset: the SPEIbase: A new gridded product for the analysis of drought variability and impacts. *Bulletin of the American Meteorological Society, 91*, 1351–1356. https://doi.org/10.1175/2010bams2988.1

Benevides, P., Catalao, J., & Miranda, P. M. A. (2015). On the inclusion of GPS precipitable water vapour in the nowcasting of rainfall. *Natural Hazards and Earth System Sciences, 15*, 2605–2616. https://doi.org/10.5194/nhess-15-2605-2015

Bevis, M., Businger, S., Chiswell, S., Herring, T. A., Anthes, R. A., Rocken, C., & Ware, R. H. (1994). Gps meteorology - mapping zenith wet delays onto precipitable water. *Journal of Applied Meteorology, 33*, 379–386. https://doi.org/10.1175/1520-0450(1994)033%3c0379:Gmmzwd%3e2.0.Co;2

Bevis, M., Businger, S., Herring, T. A., Rocken, C., Anthes, R. A., & Ware, R. H. (1992). Gps meteorology - remote-sensing of atmospheric water-vapor using the global positioning system. *Journal of Geophysical Research-Atmospheres, 97*, 15787–15801. https://doi.org/10.1029/92jd01517

Bordi, I., Raziei, T., Pereira, L. S., & Sutera, A. (2014). Ground-Based GPS measurements of precipitable water vapor and their usefulness for hydrological applications. *Water Resources Management, 29*, 471–486. https://doi.org/10.1007/s11269-014-0672-5

Bordi, I., Zhu, X., & Fraedrich, K. (2015). Precipitable water vapor and its relationship with the standardized precipitation index: Ground-based GPS measurements and reanalysis data. *Theoretical and Applied Climatology, 123*, 263–275. https://doi.org/10.1007/s00704-014-1355-0

Chung, E. S., Soden, B., Sohn, B. J., & Shi, L. (2014). Upper-tropospheric moistening in response to anthropogenic warming. *Proc Natl Acad Sci U S A, 111*, 11636–11641. https://doi.org/10.1073/pnas.1409659111

Dai, M., Huang, S., Huang, Q., Zheng, X., Su, X., Leng, G., Li, Z., Guo, Y., Fang, W., & Liu, Y. J. (2022). Propagation characteristics and mechanism from meteorological to agricultural drought in various seasons. *Journal of Hydrology, 610*, 127897. https://doi.org/10.1016/j.jhydrol.2022.127897

Diffenbaugh, N. S., Singh, D., Mankin, J. S., Horton, D. E., Swain, D. L., Touma, D., Charland, A., Liu, Y., Haugen, M., Tsiang, M., & Rajaratnam, B. (2017). Quantifying the influence of global warming on unprecedented extreme climate events. *Proc Natl Acad Sci U S A, 114*, 4881–4886. https://doi.org/10.1073/pnas.1618082114

Ding, Y., Gong, X., Xing, Z., Cai, H., Zhou, Z., Zhang, D., Sun, P., & Shi, H. (2021). Attribution of meteorological, hydrological and agricultural drought propagation in different climatic regions of China. *Agricultural Water Management, 255*, 106996. https://doi.org/10.1016/j.agwat.2021.106996

Doswell, C. A., Brooks, H. E., & Maddox, R. A. (1996). Flash flood forecasting: An ingredients-based methodology. *Weather and Forecasting, 11*, 560–581. https://doi.org/10.1175/1520-0434(1996)011%3c0560:Fffaib%3e2.0.Co;2

Durre, I., Xungang, Y., Vose, R. S., Applequist, S., & Arnfield, J. (2016). Integrated global radiosonde archive (IGRA), Version 2. *NOAA National Centers for Environmental Information*. https://doi.org/10.7289/V5X63K0Q

Gao, B.-C., & Kaufman, Y. J. (2003). Water vapor retrievals using moderate resolution imaging spectroradiometer MODIS near-infrared channels. *Journal of Geophysical Research Atmospheres*. https://doi.org/10.1029/2002JD003023

Gui, K., Che, H., Chen, Q., Zeng, Z., Liu, H., Wang, Y., Zheng, Y., Sun, T., Liao, T., Wang, H., & Zhang, X. (2017). Evaluation of radiosonde, MODIS-NIR-Clear, and AERONET precipitable water vapor using IGS ground-based GPS measurements over China. *Atmospheric Research, 197*, 461–473. https://doi.org/10.1016/j.atmosres.2017.07.021

He, Y., Lin, K., Tang, G., Chen, X., Guo, S., & Gui, F. (2017). Quantifying the changing properties of climate extremes in Guangdong Province using individual and integrated climate indices. *International Journal of Climatology, 37*, 781–792. https://doi.org/10.1002/joc.4739

Hersbach, H., Bell, B., Berrisford, P., Hirahara, S., Horanyi, A., Munoz-Sabater, J., Nicolas, J., Peubey, C., Radu, R., Schepers, D., Simmons, A., Soci, C., Abdalla, S., Abellan, X., Balsamo, G., Bechtold, P., Biavati, G., Bidlot, J., Bonavita, M., … Thepaut, J. N. (2020). The ERA5 global reanalysis. *Quarterly Journal of the Royal Meteorological Society, 146*, 1999–2049. https://doi.org/10.1002/qj.3803

Zhu et al. Satellite Navigation   *(2024) 5:1*

Page 16 of 17

Huang, L., Mo, Z., Xie, S., Liu, L., Chen, J., Kang, C., & Wang, S. (2021). Spatiotemporal characteristics of GNSS-derived precipitable water vapor during heavy rainfall events in Guilin China. *Satellite Navigation, 2*, 13. https://doi.org/10.1186/s43020-021-00046-y

Ingram, W. (2010). A very simple model for the water vapour feedback on climate change. *Quarterly Journal of the Royal Meteorological Society, 136*, 30–40. https://doi.org/10.1002/qj.546

Jacob, D. (2001). The role of water vapour in the atmosphere. A short overview from a climate modeller's point of view. *Physics and Chemistry of the Earth Part a-Solid Earth and Geodesy, 26*, 523–527. https://doi.org/10.1016/S1464-1895(01)00094-1

Jadala, N. B., Sridhar, M., Dutta, G., Yousuf, M., & Reddy, Y. K. (2022). Integrated water vapor during active and break spells of monsoon and its relationship with temperature, precipitation and precipitation efficiency over a tropical site. *Geodesy and Geodynamics, 13*, 238–246. https://doi.org/10.1016/j.geog.2021.09.008

Jade, S., Vijayan, M. S. M., Gaur, V. K., Prabhu, T. P., & Sahu, S. C. (2005). Estimates of precipitable water vapour from GPS data over the Indian subcontinent. *Journal of Atmospheric and Solar-Terrestrial Physics, 67*, 623–635. https://doi.org/10.1016/j.jastp.2004.12.010

Karl, T. R., Gleason, B. E., Menne, M. J., McMahon, J. R., Heim, R. R., Brewer, M. J., Kunkel, K. E., Arndt, D. S., Privette, J. L., Bates, J. J., Groisman, P. Y., & Easterling, D. R. (2012). U.S. temperature and drought: Recent anomalies and trends. *Eos, Transactions American Geophysical Union, 93*, 473–474. https://doi.org/10.1029/2012eo470001

Li, H., Wan, Q., Peng, D., Liu, X., & Xiao, H. (2020a). Multiscale analysis of a record-breaking heavy rainfall event in Guangdong. *China. Atmospheric Research, 232*, 104703. https://doi.org/10.1016/j.atmosres.2019.104703

Li, Q., He, P., He, Y., Han, X., Zeng, T., Lu, G., & Wang, H. (2020b). Investigation to the relation between meteorological drought and hydrological drought in the upper Shaying River Basin using wavelet analysis. *Atmospheric Research, 234*, 104743. https://doi.org/10.1016/j.atmosres.2019.104743

Li, R. L., Studholme, J. H. P., Fedorov, A. V., & Storelvmo, T. (2022). Precipitation efficiency constraint on climate change. *Nature Climate Change, 12*, 642–648. https://doi.org/10.1038/s41558-022-01400-x

Li, R. L., Studholme, J. H. P., Fedorov, A. V., & Storelvmo, T. (2023). Increasing precipitation efficiency amplifies climate sensitivity by enhancing tropical circulation slowdown and eastern pacific warming pattern. *Geophysical Research Letters*. https://doi.org/10.1029/2022gl100836

Li, X., Zus, F., Lu, C., Dick, G., Ning, T., Ge, M., Wickert, J., & Schuh, H. (2015). Retrieving of atmospheric parameters from multi-GNSS in real time: Validation with water vapor radiometer and numerical weather model. *Journal of Geophysical Research-Atmospheres, 120*, 7189–7204. https://doi.org/10.1002/2015jd023454

Li, Z., Muller, J. P., & Cross, P. (2003). Comparison of precipitable water vapor derived from radiosonde, GPS, and Moderate-Resolution Imaging Spectroradiometer measurements. *Journal of Geophysical Research-Atmospheres*. https://doi.org/10.1029/2003jd003372

Liu, C., Zhang, Q., Singh, V. P., & Cui, Y. (2011). Copula-based evaluations of drought variations in Guangdong, South China. *Natural Hazards, 59*, 1533–1546. https://doi.org/10.1007/s11069-011-9850-4

Liu, Z., Wong, M., Nichol, J., & Chan, P. (2013). A multi-sensor study of water vapour from radiosonde, MODIS and AERONET: A case study of Hong Kong. *International Journal of Climatology, 33*, 109–120. https://doi.org/10.1002/joc.3412

Ma, X., Yao, Y., & Zhao, Q. (2021). Regional GNSS-derived SPCI: Verification and improvement in Yunnan. *China. Remote Sensing, 13*, 1918. https://doi.org/10.3390/rs13101918

McKee TB, Doesken NJ, Kleist J. (1993). The relationship of drought frequency and duration to time scales. Paper presented at the Proceedings of the 8th Conference on Applied Climatology

Ming, F., Yang, Y. X., Zeng, A. M., & Zhao, B. (2017). Spatiotemporal filtering for regional GPS network in China using independent component analysis. *Journal of Geodesy, 91*, 419–440. https://doi.org/10.1007/s00190-016-0973-y

O'Gorman, P. A. (2015). Precipitation extremes under climate change. *Current Climate Change Reports, 1*, 49–59. https://doi.org/10.1007/s40641-015-0009-3

O'Gorman, P. A., & Schneider, T. (2009). The physical basis for increases in precipitation extremes in simulations of 21st-century climate change.

Proceedings of the National Academy of Sciences, 106, 14773–14777. https://doi.org/10.1073/pnas.0907610106

Ohtani, R., & Naito, I. (2000). Comparisons of GPS-derived precipitable water vapors with radiosonde observations in Japan. *Journal of Geophysical Research-Atmospheres, 105*, 26917–26929. https://doi.org/10.1029/2000jd900362

Pall, P., Allen, M. R., & Stone, D. A. (2007). Testing the Clausius-Clapeyron constraint on changes in extreme precipitation under CO2 warming. *Climate Dynamics, 28*, 351–363. https://doi.org/10.1007/s00382-006-0180-2

Rocken, C., Van Hove, T., & Ware, R. (1997). Near real-time GPS sensing of atmospheric water vapor. *Geophysical Research Letters, 24*, 3221–3224. https://doi.org/10.1029/97gl03312

Rodell, M., Houser, P. R., Jambor, U., Gottschalck, J., Mitchell, K., Meng, C. J., Arsenault, K., Cosgrove, B., Radakovich, J., Bosilovich, M., Entin, J. K., Walker, J. P., Lohmann, D., & Toll, D. (2004). The global land data assimilation system. *Bulletin of the American Meteorological Society, 85*, 381–394. https://doi.org/10.1175/Bams-85-3-381

Schneider, T., O'Gorman, P. A., & Levine, X. J. (2010). Water vapor and the dynamics of climate changes. *Reviews of Geophysics*. https://doi.org/10.1029/2009rg000302

Sedgwick, P. (2012). Pearson's correlation coefficient. *British Medical Journal, 344*, e4483. https://doi.org/10.1136/bmj.e4483

Shi C, Zhao Q, Geng J, Lou Y, Ge M, Liu J. (2008). Recent development of PANDA software in GNSS data processing. Paper presented at the International Conference on Earth Observation Data Processing and Analysis (ICEODPA). doi: https://doi.org/10.1117/12.816261.

Stott, P. (2016). CLIMATE CHANGE. How climate change affects extreme weather events. *Science, 352*, 1517–1518. https://doi.org/10.1126/science.aaf7271

Sui, C., Li, X., & Yang, M. (2007). On the definition of precipitation efficiency. *Journal of the Atmospheric Sciences, 64*, 4506–4513. https://doi.org/10.1175/2007jas2332.1

Thomas, A. C., Reager, J. T., Famiglietti, J. S., & Rodell, M. (2014). A GRACE-based water storage deficit approach for hydrological drought characterization. *Geophysical Research Letters, 41*, 1537–1545. https://doi.org/10.1002/2014gl059323

Trenberth, K. E., Dai, A., Rasmussen, R. M., & Parsons, D. B. (2003). The changing character of precipitation. *Bulletin of the American Meteorological Society, 84*, 1205–1217. https://doi.org/10.1175/Bams-84-9-1205

Tuller, S. E. (1971). The world distribution of annual precipitation efficiency. *Journal of Geography, 70*, 219–223. https://doi.org/10.1080/00221347108981623

Tuller, S. E. (1973). Seasonal and annual precipitation efficiency in Canada. *Atmosphere, 11*, 52–66. https://doi.org/10.1080/00046973.1973.9648348

Van Loon, A. F. (2015). Hydrological drought explained. WIREs. *Water, 2*, 359–392. https://doi.org/10.1002/wat2.1085

Vicente-Serrano, S. M., Begueria, S., & Lopez-Moreno, J. I. (2010). A multiscalar drought index sensitive to global warming: The standardized precipitation evapotranspiration index. *Journal of Climate, 23*, 1696–1718. https://doi.org/10.1175/2009jcli2909.1

Vicente-Serrano, S. M., Lopez-Moreno, J. I., Begueria, S., Lorenzo-Lacruz, J., Sanchez-Lorenzo, A., Garcia-Ruiz, J. M., Azorin-Molina, C., Moran-Tejeda, E., Revuelto, J., Trigo, R., Coelho, F., & Espejo, F. (2014). Evidence of increasing drought severity caused by temperature rise in southern Europe. *Environmental Research Letters, 9*, 044001. https://doi.org/10.1088/1748-9326/9/4/044001

Wang, D., Wang, X., Liu, L., Wang, D., Huang, H., & Pan, C. (2016a). Evaluation of CMPA precipitation estimate in the evolution of typhoon-related storm rainfall in Guangdong, China. *Journal of Hydroinformatics, 18*, 1055–1068. https://doi.org/10.2166/hydro.2016.241

Wang, J., Dai, A., & Mears, C. (2016b). Global water vapor trend from 1988 to 2011 and its diurnal asymmetry based on gps, radiosonde, and microwave satellite measurements. *Journal of Climate, 29*, 5205–5222. https://doi.org/10.1175/Jcli-D-15-0485.1

Wang, J., Gui, S., Ma, A., Yang, R., & Zhang, Q. (2019). Interdecadal variability of summer precipitation efficiency in East Asia. *Advances in Meteorology, 2019*, 3563024. https://doi.org/10.1155/2019/3563024

Wang, X., Zhang, K., Wu, S., Fan, S., & Cheng, Y. (2016c). Water vapor-weighted mean temperature and its impact on the determination of precipitable water vapor and its linear trend. *Journal of Geophysical*

Zhu et al. Satellite Navigation   *(2024) 5:1*

Page 17 of 17

Research-Atmospheres, 121, 833–852. https://doi.org/10.1002/2015j
d024181

Wessel, P., Luis, J. F., Uieda, L., Scharroo, R., Wobbe, F., Smith, W. H. F., & Tian, D.
(2019). The generic mapping tools version 6. *Geochemistry Geophysics
Geosystems, 20*, 5556–5564. https://doi.org/10.1029/2019gc008515

Wu, J., Chen, X., Yao, H., & Zhang, D. (2021). Multi-timescale assessment of
propagation thresholds from meteorological to hydrological drought.
Science of the Total Environment, 765, 144232. https://doi.org/10.1016/j.
scitotenv.2020.144232

Yao, C., Shum, C. K., Luo, Z., Li, Q., Lin, X., Xu, C., Zhang, Y., Chen, J., Huang, Q.,
& Chen, Y. (2022). An optimized hydrological drought index integrating
GNSS displacement and satellite gravimetry data. *Journal of Hydrology,
614*, 128647. https://doi.org/10.1016/j.jhydrol.2022.128647

Ye, H., Fetzer, E. J., Wong, S., Behrangi, A., Olsen, E. T., Cohen, J., Lambrigtsen,
B. H., & Chen, L. (2014). Impact of increased water vapor on precipita-
tion efficiency over northern Eurasia. *Geophysical Research Letters, 41*,
2941–2947. https://doi.org/10.1002/2014gl059830

Yi, S., & Sneeuw, N. (2021). Filling the data gaps within GRACE missions using
singular spectrum analysis. *Journal of Geophysical Research-Solid Earth*.
https://doi.org/10.1029/2020JB021227

Yin, L., Ping, F., Mao, J., & Jin, S. (2022). Analysis on precipitation efficiency of
the "21.7" henan extremely heavy rainfall event. *Advances in Atmospheric
Sciences, 40*, 374–392. https://doi.org/10.1007/s00376-022-2054-x

Zhai, P., Yu, R., Guo, Y., Li, Q., Ren, X., Wang, Y., Xu, W., Liu, Y., & Ding, Y. (2016). The
strong El Nino of 2015/16 and its dominant impacts on global and china's
climate. *Journal of Meteorological Research, 30*, 283–297. https://doi.org/
10.1007/s13351-016-6101-3

Zhang, B., & Yao, Y. (2021). Precipitable water vapor fusion based on a general-
ized regression neural network. *Journal of Geodesy, 95*, 36. https://doi.org/
10.1007/s00190-021-01482-z

Zhang, Q., Ye, J., Zhang, S., & Han, F. (2018). Precipitable water vapor retrieval
and analysis by multiple data sources: ground-based GNSS, radio occulta-
tion, radiosonde, microwave satellite, and NWP reanalysis data. *Journal of
Sensors, 2018*, 3428303. https://doi.org/10.1155/2018/3428303

Zhao, Q., Liu, Y., Ma, X., Yao, W., Yao, Y., & Li, X. (2020a). An improved rainfall
forecasting model based on GNSS observations. *IEEE Transactions on
Geoscience and Remote Sensing, 58*, 4891–4900. https://doi.org/10.1109/
Tgrs.2020.2968124

Zhao, Q., Ma, X., Yao, W., Liu, Y., & Yao, Y. (2020b). A Drought monitoring method
based on precipitable water vapor and precipitation. *Journal of Climate,
33*, 10727–10741. https://doi.org/10.1175/Jcli-D-19-0971.1

Zhao, Q., Zhang, X., Wu, K., Liu, Y., Li, Z., & Shi, Y. (2022). Comprehensive precipi-
table water vapor retrieval and application platform based on various
water vapor detection techniques. *Remote Sensing, 14*, 2507. https://doi.
org/10.3390/rs14102507

Zhou, Z., Shi, H., Fu, Q., Ding, Y., Li, T., & Liu, S. (2021). Investigating the propaga-
tion from meteorological to hydrological drought by introducing the
nonlinear dependence with directed information transfer index. *Water
Resources Research*. https://doi.org/10.1029/2021WR030028

Zhou, Z., Shi, H., Fu, Q., Ding, Y., Li, T., Wang, Y., & Liu, S. (2021). Characteristics of
propagation from meteorological drought to hydrological drought in the
Pearl River Basin. *Journal of Geophysical Research-Atmospheres*. https://doi.
org/10.1029/2020JD033959

Zhu, H., Chen, K., Hu, S., Liu, J., Shi, H., Wei, G., Chai, H., Li, J., & Wang, T. (2023).
*Using the global navigation satellite system and precipitation data to
establish the propagation characteristics of meteorological and hydrological
Drought in Yunnan*. Water Resources Research. https://doi.org/10.1029/
2022WR033126

Zhu, H., Chen, K., Hu, S., Wei, G., Chai, H., & Wang, T. (2023b). Characterizing
hydrological droughts within three watersheds in Yunnan, China from
GNSS-inferred terrestrial water storage changes constrained by GRACE
data. *Geophysical Journal International, 235*, 1581–1599. https://doi.org/10.
1093/gji/ggad321

Publisher's Note